

**LDA+DMFT approach to core-level spectroscopy: Application to 3d transition metal compounds**Atsushi Hariki,<sup>1</sup> Takayuki Uozumi,<sup>2</sup> and Jan Kuneš<sup>1</sup><sup>1</sup>*Institute for Solid State Physics, TU Wien, 1040 Vienna, Austria*<sup>2</sup>*Department of Mathematical Sciences, Graduate School of Engineering, Osaka Prefecture University 1-1 Gakuen-cho, Nakaku, Sakai, Osaka 599-8531, Japan*

(Received 6 April 2017; revised manuscript received 19 June 2017; published 13 July 2017)

We present a computational study of 2p core-level x-ray photoemission spectra of transition metal monoxides  $MO$  ( $M = \text{Ni, Co, Mn}$ ) and sesquioxides  $M_2O_3$  ( $M = \text{V, Cr, Fe}$ ) using a theoretical framework based on the local-density approximation + dynamical mean-field theory. We find a very good description of the fine spectral features, which is a considerable improvement over the conventional cluster model. We analyze the role of nonlocal screening and its relationship to long-range magnetic order and lattice geometry. Our results reveal the potential of the present method for the analysis and interpretation of modern high-energy-resolution experiments.

DOI: [10.1103/PhysRevB.96.045111](https://doi.org/10.1103/PhysRevB.96.045111)**I. INTRODUCTION**

Materials with strongly correlated electrons possess a number of fascinating phenomena ranging from high-temperature superconductivity to exotic orders of spin, orbit, and charge degrees of freedom. A microscopic understanding of the complex interplay between the formation of atomic multiplets and interatomic hybridization—chemical bonding—is one of the challenging topics in condensed-matter physics [1,2]. Core-level x-ray spectroscopy is a powerful tool in the investigation of strongly correlated materials [3]. The past decade witnessed great advances in high-resolution and bulk-sensitive techniques for first-order optical processes, such as x-ray photoemission spectroscopy (XPS) with hard-x-ray ( $>5$  keV) [4–11] as well as resonant inelastic x-ray scattering (RIXS) [12,13]. The experimental progress paved the way for fine spectral features reflecting low-energy physics, e.g., elementary magnetic excitations [14–16].

Theoretical modeling is a crucial step in inferring microscopic physics from experimental spectra. With XPS, the system is probed through a response to the core hole created by x-ray irradiation. The core hole, e.g., in the 2p shell of a transition metal (TM), strongly interacts with localized 3d electrons, which leaves a fingerprint of the atomic multiplet structure in the spectra. In addition, the core hole presents charge and spin perturbation, which induces a dynamical response of the valence electrons. This response is traditionally referred to as charge-transfer (CT) screening. The CT screening effectively amplifies the effect of hybridization of the excited atom with its surroundings in the core-level XPS.

The  $MO_6$  cluster model (CM) is probably the most popular model that has been conventionally employed to analyze x-ray spectra of TM compounds since the 1980s [17–19]. In this model, the intra-atomic interactions on the TM site and hybridization of the TM 3d states with neighboring ligands are considered, while the rest of the lattice consisting of the ligand and TM atoms is neglected. The CM has been very successful in explaining the overall structure of the XPS and x-ray absorption spectra of numerous TM compounds. However, its limitations when it comes to the fine spectral features became obvious with the arrival of high-resolution experiments. For example, it fails to reproduce the fine structure of the  $2p_{3/2}$  main line (ML) observed in a series of transition metal oxides

(TMOs) [4–11]. A similar failure of the CM was reported for other excitation processes, such as  $L$ -edge RIXS in TMOs [20]. It was proposed that the failure results from the absence of the CT process beyond the nearest-neighbor ligands, in particular from the other TM atoms, referred to as nonlocal screening (NLS) [21]. The NLS involves many-body states, including the TM neighbors, which are responsible for the low-energy physics of spin and orbital ordering [22–24]. Thus, it allows the core-level XPS to probe nonlocal phenomena as well.

For the theory to keep up with high-resolution experiments, it is important to introduce a framework that overcomes the limitations of the CM analysis. In this article, we present a systematic study of 2p XPS spectra of selected 3d compounds based on the local-density approximation (LDA) + dynamical mean-field theory (DMFT) [25,26]. The present approach [23,27] consists in postprocessing of the LDA+DMFT calculations, in which the Anderson impurity model (AIM) with the DMFT hybridization functions is extended to include explicitly the core orbitals and their interaction with TM 3d orbitals. Technically, the discrete ligand states of the CM are replaced by a continuous DMFT bath, which contains information about the entire lattice. In addition to the conceptual advance, the method eliminates some of the ambiguities in the choice of CM parameters, which are replaced by the LDA+DMFT calculation [28,29]. To calculate the spectra of the extended AIM, an impurity solver based on the configuration-interaction scheme was developed [24,30].

Previously, some of us applied the described approach to the  $2p_{3/2}$  XPS in cuprates, NiO, and  $\text{La}_{1-x}\text{Sr}_x\text{MnO}_3$  [23,24,27]. A close relationship of the experimental features of the  $2p_{3/2}$  peak to the many-body composite structure of the top of the valance band, such as the Zhang-Rice band, and long-range spin-orbit order was pointed out. Here, we report a systematic analysis of 2p XPS spectra of  $MO$  ( $M = \text{Ni, Co, Mn}$ ) and  $M_2O_3$  systems ( $M = \text{V, Cr, Fe}$ ) for which high-resolution HAXPES data exist. We pay special attention to the NLS. We discuss how the fine spectral features are related to the material-specific properties, such as the metallicity of  $\text{V}_2\text{O}_3$ ; the magnetic order of NiO, CoO, and  $\text{Fe}_2\text{O}_3$ ; or the crystal geometry, upon which the NLS is shown to depend sensitively. Our results show that NLS is a common contributing factor to

the core-level XPS spectra of TMO, and it must be taken into account when interpreting the spectra.

## II. THEORETICAL METHOD

In photoemission spectroscopy, a photon is absorbed while an electron-hole pair is created. Since the electron leaves the sample and thus does not interact with the hole left behind, the photoemission spectrum reflects the hole dynamics described by the one-particle Green function. In core-level XPS, a further simplification comes from the fact that the core hole does not move. Obtaining a theoretical description of the core-level XPS consists in dressing the core-hole Green function, for which the term “screening” is traditionally used in the context of core-level spectroscopy. Since the core hole is immobile, a description in terms of the quantum impurity model appears natural. The DMFT provides a systematic approach to construct such a model.

The calculation of the core-level spectra proceeds in three steps: (i) construction of a  $dp$  model from the converged LDA calculation, (ii) solution of the DMFT self-consistent equation for the  $dp$  model to obtain the DMFT hybridization function, and (iii) calculation of the core-level spectra using the extended AIM with the DMFT hybridization function. Steps (i) and (ii) are standard for the LDA+DMFT method. In DMFT, the local correlations are included explicitly while the nonlocal correlations are included only on the static mean-field level [26]. The core of the method is mapping of the lattice problem onto an AIM with a self-consistently determined hybridization function  $V^2(\varepsilon)$  [31].  $V^2(\varepsilon)$  is in general a matrix in the orbital and spin indices. For a  $d$  shell in a cubic environment, it becomes diagonal in the  $e_g/t_{2g}$  basis. This is exactly the case in the paramagnetic phases of the monoxides and approximately so in the AF phases and in the sesquioxides. We neglect the small off-diagonal elements of  $V^2(\varepsilon)$  in the latter throughout this study and consider only the diagonal elements. The orbital- and spin-diagonal hybridization density  $V(\varepsilon)$  on the real-energy axis is given by [23,26]

$$V_{\gamma\sigma}^2(\varepsilon) = -\frac{1}{\pi} \text{Im} \langle d_{\gamma\sigma} | [\varepsilon - h^0 - \Sigma(\varepsilon) - G^{-1}(\varepsilon)] | d_{\gamma\sigma} \rangle, \quad (1)$$

where  $\Sigma(\varepsilon)$ ,  $G(\varepsilon)$ , and  $h^0$  are the local self-energy, the local Green's function, and the one-body part of the on-site Hamiltonian, respectively. The  $\gamma$  and  $\sigma$  denote orbital and spin indices.

In step (i), we perform an LDA calculation with the WIEN2K package [32] for the experimental lattice parameters. The LDA bands of the TM  $3d$  and O  $2p$  are mapped onto a  $dp$  tight-binding (TB) model using the WIEN2WANNIER interface [33] and the WANNIER90 code [34]. The spin-orbit (SO) interaction within the  $3d$  shell turned out to have a negligible effect on the studied spectra, and the presented results were obtained without it. When necessary, the inclusion of the SO interaction in the  $dp$  model is straightforward [33].

In step (ii), the TB model is augmented with the two-particle Coulomb interaction within the TM  $3d$  shell, and DMFT is employed to iteratively calculate the local self-energy and the hybridization function. Merging the LDA with many-body approaches suffers from the well-known problem of how to

avoid double counting the interaction terms. In this work, we renormalize the  $3d$  site energies by a constant shift  $\mu_d$  treated as an adjustable parameter. A long-range order, e.g., antiferromagnetic (AF) spin order, may develop if the spin dependence of the self-energy and the proper magnetic unit cell are allowed. We use the continuous-time quantum Monte Carlo method (CT-QMC) in the hybridization expansion algorithm [35,36] at this step. The CT-QMC calculation is performed using a standard code [24,30] based on the segment picture with recent improved estimator techniques [37,38], with the density-density form of the Coulomb interaction used for computational efficiency. The Coulomb interaction between  $3d$  electrons is parametrized by  $U = F_0$  and  $J = (F_2 + F_4)/14$ , where  $F_0$ ,  $F_2$ , and  $F_4$  are the Slater integrals [39,40]. The configuration-averaged Coulomb interaction  $U_{dd}$  is given as  $U_{dd} = U - 4J/9$ . Once the self-consistency is achieved, self-energy  $\Sigma(\varepsilon)$  on the real frequency axis is computed by analytic continuation using the maximum-entropy method [41,42].

Next, we construct the extended AIM. The hybridization density for real frequencies is obtained from (1) and approximated by 25 bath states, which provides reasonable consistency with the CT-QMC data.

The AIM is augmented with the  $2p$  core states. The  $2p$ - $3d$  interaction is parametrized with the Slater integrals. The full form of the Coulomb  $3d$ - $3d$  and  $2p$ - $3d$  interaction is considered at this step with the same coupling constants as used in the DMFT calculation.

The  $2p$  XPS spectral function for the binding energy  $E_B$  is given by [3]

$$F_{\text{XPS}}(E_B) = -\frac{1}{\pi} \text{Im} \sum_n \langle n | \hat{c}^\dagger \frac{1}{E_B + E_n - \hat{H}} \hat{c} | n \rangle \frac{e^{-E_n/k_B T}}{Z} \\ = \sum_n F_{\text{XPS}}^n \frac{e^{-E_n/k_B T}}{Z}, \quad (2)$$

where  $E_n$  is the eigenenergy of the  $n$ th excited states  $|n\rangle$ , and  $e^{-E_n/k_B T}/Z$  is the corresponding Boltzmann factor with the partition function  $Z$ .  $F_{\text{XPS}}^n$  represents the individual contribution of the  $n$ th excited state in the initial state to the XPS spectra. The operator  $\hat{c}$  creates a  $2p$  core hole at the impurity TM site. The spectral function is calculated using the Lanczos algorithm within a configuration-interaction scheme [30].

The impurity Hamiltonian  $\hat{H}$  has the form

$$\hat{H} = \hat{H}_{\text{TM}} + \hat{H}_{\text{hyb}}, \quad (3)$$

where  $\hat{H}_{\text{hyb}}$  describes hybridization with the fermionic bath [43]. The on-site Hamiltonian  $\hat{H}_{\text{TM}}$  is given as

$$\hat{H}_{\text{TM}} = \sum_{\gamma,\sigma} \tilde{\varepsilon}_d(\gamma) \hat{d}_{\gamma\sigma}^\dagger \hat{d}_{\gamma\sigma} + U_{dd} \sum_{\gamma\sigma > \gamma'\sigma'} \hat{d}_{\gamma\sigma}^\dagger \hat{d}_{\gamma\sigma} \hat{d}_{\gamma'\sigma'}^\dagger \hat{d}_{\gamma'\sigma'} \\ - U_{dc} \sum_{\gamma,\sigma,\zeta,\eta} \hat{d}_{\gamma\sigma}^\dagger \hat{d}_{\gamma\sigma} (1 - \hat{c}_{\zeta\eta}^\dagger \hat{c}_{\zeta\eta}) + \hat{H}_{\text{multiplet}}. \quad (4)$$

Here,  $\hat{d}_{\gamma\sigma}^\dagger$  ( $\hat{d}_{\gamma\sigma}$ ) and  $\hat{c}_{\zeta\eta}^\dagger$  ( $\hat{c}_{\zeta\eta}$ ) are the electron creation (annihilation) operators for TM  $3d$  and  $2p$  electrons, respectively. The  $\gamma$  ( $\zeta$ ) and  $\sigma$  ( $\eta$ ) are the TM  $3d$  ( $2p$ ) orbital and the spin indices. The TM  $3d$  site energies  $\tilde{\varepsilon}_d(\gamma) = \varepsilon_d(\gamma) - \mu_d$  are the energies of the Wannier states  $\varepsilon_d(\gamma)$  shifted by the double-counting

TABLE I. Coulomb interaction  $U$ , Hund's interaction  $J$ , core-hole potential  $U_{dc}$ , and double-counting correction  $\mu_d$  used in the studied compounds (in eV).

	NiO	CoO	MnO	V <sub>2</sub> O <sub>3</sub>	Fe <sub>2</sub> O <sub>3</sub>	Cr <sub>2</sub> O <sub>3</sub>	LaCrO <sub>3</sub>
$U$	7.0	7.3	7.0	4.8	6.8	7.0	7.0
$J$	1.1	1.1	0.95	0.7	0.86	0.8	0.8
$U_{dc}$	7.8	8.6	8.5	6.5	8.4	9.0	9.0
$\mu_d$	52.0	47.6	30.5	8.1	30.6	23.6	23.8

correction  $\mu_d$ . The isotropic parts of the  $3d$ - $3d$  ( $U_{dd}$ ) and  $2p$ - $3d$  ( $U_{dc}$ ) interactions are shown explicitly, while terms containing higher Slater integrals and the SO interaction are contained in  $\tilde{H}_{\text{multiplet}}$ .

### A. Computational parameters

The parameters in the present approach are the  $3d$ - $3d$  and  $2p$ - $3d$  interaction constants and the double-counting correction  $\mu_d$ . We used the typical values of the  $3d$ - $3d$   $U, J$  interaction parameters reported for transition metal oxides obtained with constraint RPA and LDA methods for NiO, CoO, MnO, Fe<sub>2</sub>O<sub>3</sub> (FeO) [44–46], and other valence XPS studies for V<sub>2</sub>O<sub>3</sub>, Cr<sub>2</sub>O<sub>3</sub>, and LaCrO<sub>3</sub> [47–49]. Some fine tuning (up to 0.25 eV for  $J$  and up to 2.0 eV for  $U$ ) was done to obtain a good match with the experimental x-ray absorption (XAS) and RIXS spectra, which will be reported elsewhere. Unlike XAS and RIXS spectra, the variation of interaction parameters on this scale has a barely observable effect on the studied core-level XPS spectra. Several *ad hoc* schemes to determine  $\mu_d$  exist in the literature. Rather than using one of these, we adjust  $\mu_d$  such that the DMFT spectral function reproduces the valence photoemission experiments. Therefore, the  $3d$ - $3d$  interaction and  $\mu_d$  are determined independent of the core-level XPS spectra. The SO coupling within the  $2p$  shell and the anisotropic part of the  $2p$ - $3d$  interaction parameters  $F^k, G^k$  [3,50] are calculated with an atomic Hartree-Fock code. The  $F^k$  and  $G^k$  values are scaled down to 75–80% of their actual values to simulate the effect of intra-atomic configuration interaction from higher basis configurations neglected in the atomic calculation, which is a successful empirical treatment [43,51–54]. The isotropic part  $U_{dc}$  is fixed by matching the splitting between the ML and CT satellite of the experimental  $2p$  XPS spectra (see Fig. 1). The actual values of  $U_{dc}$  fulfill the empirical rule  $U_{dc} \approx 1.3U_{dd}$  [17,19,43,55,56] within 15% accuracy. We point out that the fine structure of ML, the main result of this study, is insensitive to the exact  $U_{dc}$  value. The values used in this study are listed in Table I.

## III. RESULTS AND DISCUSSION

The LDA+DMFT simulations were performed for typical parameters similar to those used in other LDA+DMFT studies. For the complete set of interaction computational parameters, see the Supplemental Material (SM) [57]. The valence TM  $3d$  and O  $2p$  spectral densities for all studied compounds are shown in the SM. Overall we find the same results as those from the previous DMFT and variational cluster approximation

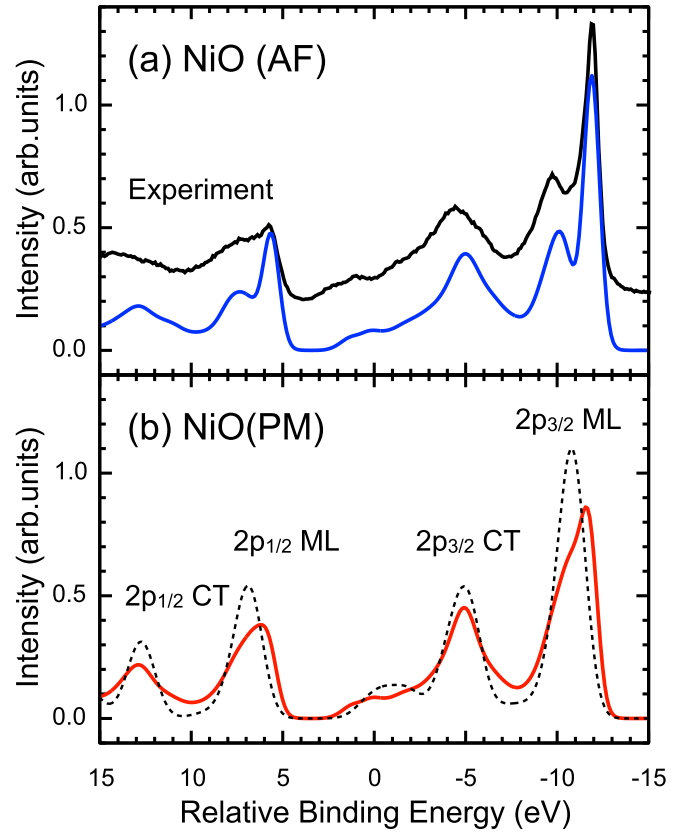


FIG. 1. The Ni  $2p$  XPS of NiO calculated for (a) AF and (b) PM phase. The experimental data in (a) are taken from Ref. [5]. The spectrum obtained by CM is shown by a dashed curve in (b) for comparison. The spectral broadening is considered using a Gaussian of 0.5 eV width (HWHM).

studies performed with the  $dp$  model: NiO [58–62], CoO [62–64], MnO [62,65,66], V<sub>2</sub>O<sub>3</sub> [47,67–69], and Fe<sub>2</sub>O<sub>3</sub> [29].

The calculations were performed for temperatures of 300 K except for the PM phase in NiO at 800 K. In addition to the comparison with experiment, we focus on an analysis of the NLS effect. While it is not possible to decompose the hybridization function into contributions of different shells of neighbors, it is possible to eliminate the TM contribution, which forms a distinct low-frequency peak. Although the weight of this peak is small relative to the rest of the hybridization function, it has a large impact on the  $2p$  XPS. The NLS is then quantified by comparing the results obtained with a full hybridization function to those obtained with a hybridization function with the low-frequency peak artificially removed. It turns out that the latter spectra closely resemble the CM results.

### A. NiO

Figures 1(a) and 1(b) show the Ni  $2p$  XPS calculated for the PM and AF phases, respectively. The large SO interaction in the  $2p$  shell splits the spectra into well-separated  $2p_{1/2}$  and  $2p_{3/2}$  parts. Each of these is separated into two peaks transitionally called the main line (ML) at lower binding energy and the charge-transfer (CT) satellite at higher binding energy. These peaks exhibit an internal fine structure, the most

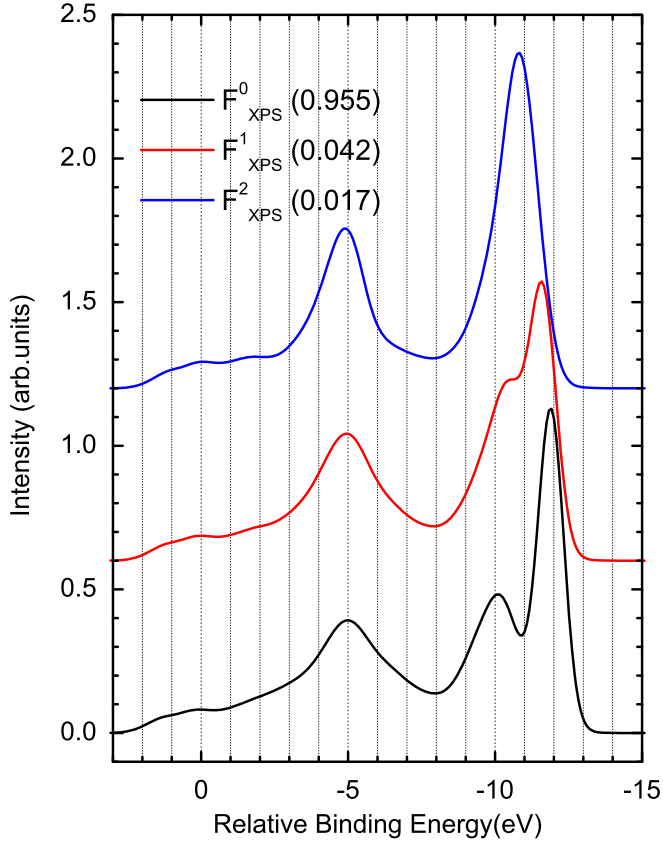


FIG. 2. The Ni  $2p_{3/2}$  spectra in the AF phase of NiO before the thermal average is summarized with the corresponding Boltzmann factors in the parentheses. The spectral broadening is considered using a Gaussian of 0.5 eV width (HWHM).

prominent of which is the double-peak  $2p_{3/2}$  ML in the AF phase. Unlike the present approach, the CM yields a sharp single-peak  $2p_{3/2}$  ML [21,55], as shown in Fig. 1(b).

Previously, some of us showed [23] that nonlocal screening (NLS) in a simplified  $d_{eg}p$  model can account for the double-peak structure. Here, we extend this result to the full  $3d$  shell and provide a more detailed discussion of the effect. Numerical experimentation with the hybridization function reveals that the low- $E_B$  peak originates from NLS from the Zhang-Rice band, while the high- $E_B$  peak is a result of local screening from neighboring O  $2p$  states [5,23]. The corresponding final states of the XPS process may be denoted  $|\underline{cd}^9\underline{D}^1\rangle$  and  $|\underline{cd}^9\underline{L}^1\rangle$ , where  $\underline{c}$ ,  $\underline{L}$ , and  $\underline{D}$  represent a hole in the Ni  $2p$  core, in the O  $2p$  band, and in the Zhang-Rice band, respectively. The  $|\underline{cd}^9\underline{L}^1\rangle$  and  $|\underline{cd}^9\underline{D}^1\rangle$  states in the many-body Hamiltonian repel each other due to the virtual hopping via the  $|\underline{cd}^8\rangle$  state. The splitting of the ML is more pronounced in the AF phase where the NLS is enhanced relative to the PM phase, as investigated in Ref. [23]. It is worth noting that the present approach also improves the description of the CT satellite over the CM result. This is because overscreened final states, such as the  $|\underline{cd}^{10}\underline{L}^1\underline{D}^1\rangle$  state, overlap with the CT satellite.

To get more insight into the NLS mechanism, Fig. 2 shows the contributions  $F_{\text{XPS}}^n$  to the AF  $2p_{3/2}$  XPS (before multiplication with Boltzmann factors) from the three lowest-energy states, which are the exchange-split members of the

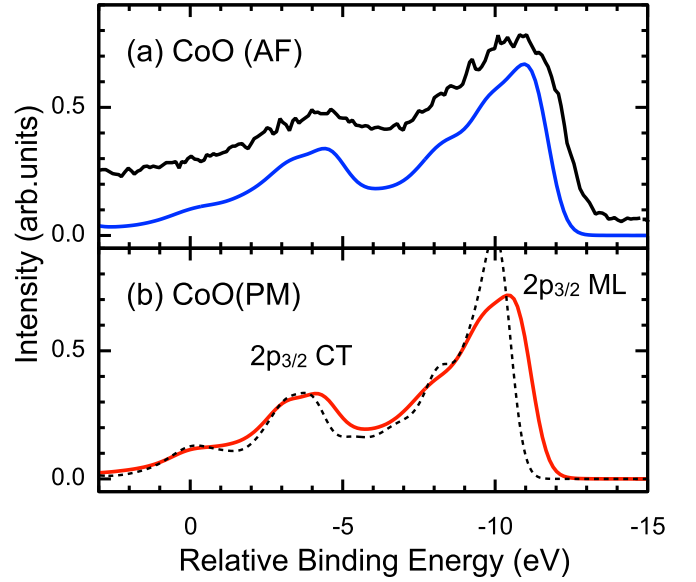


FIG. 3. The Co  $2p_{3/2}$  XPS calculated for (a) AF and (b) PM phase at 300 K. The spectrum obtained by CM is shown by a dashed curve in (b) for comparison. The spectral broadening using a Gaussian of 0.5 eV width (HWHM) is considered. The experimental data in (c) are taken from Ref. [71].

$S = 1$  triplet [70]. While the splitting of ML is very distinct in the ground-state contribution  $F_{\text{XPS}}^0$ , the two peaks get closer to each other in  $F_{\text{XPS}}^1$ . In  $F_{\text{XPS}}^2$  with  $S_z = -1$  character of  $|n\rangle$ , the ML becomes a single peak because NLS from the polarized Zhang-Rice states is forbidden by the Pauli principle. In NiO at 300 K the effect of thermal averaging is minor and the spectrum is dominated by the ground state. That this is not always the case even in insulators is shown by our next example, CoO.

## B. CoO

In Fig. 3, we compare Co  $2p_{3/2}$  XPS in CoO for (a) AF and (b) PM phase obtained in the present approach, with the experimental spectra [71] and with the CM calculation. The NLS from the states at the valence-band top, absent in the CM description, leads to broadening of the ML, but unlike in NiO it does not produce any distinct peaks. Indeed, hard-x-ray measurements found an anomalously broad  $2p_{3/2}$  ML with the shoulder in spite of high-energy resolution [71]. Comparing the spectra in the AF and PM phases, we find only a minor dependence on the magnetic order, which is consistent with the measurements across  $T_N$  [72].

Figure 4 shows the contributions to the  $2p_{3/2}$  spectra before the thermal average with the Boltzmann weights. The  $F_{\text{XPS}}^0$  in CoO shows a single-peak ML with a steplike high- $E_B$  tail. The difference from NiO is mainly due to the richer multiplet structure for  $\text{Co}^{2+}$  than  $\text{Ni}^{2+}$  [73,74]. Next, we observe a shift of the  $F_{\text{XPS}}^n$  maxima toward higher  $E_B$  in the spectra of the excited states. This is attributed to a suppression of the NLS effect in the excited states by the same argument as in NiO. The NLS-induced shift together with thermal averaging is therefore instrumental in the formation of the broad ML observed in the  $2p$  XPS experiments.



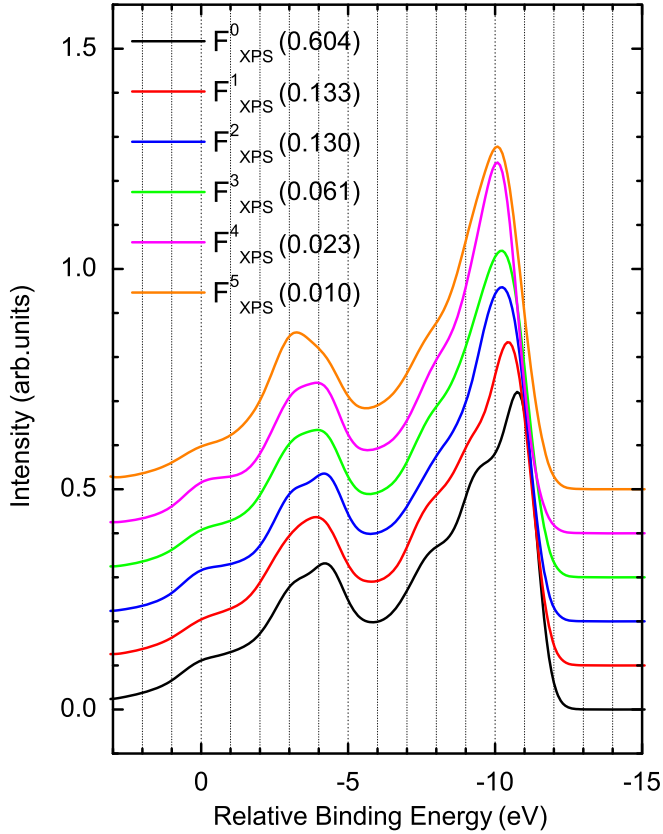


FIG. 4. The Co  $2p_{3/2}$  spectra in the AF phase before the thermal average. The corresponding Boltzmann factors at 300 K are shown in the parentheses. The spectral broadening is considered using a Gaussian of 0.5 eV width (HWHM).

### C. MnO

In Fig. 5(a) we compare the calculated Mn  $2p$  XPS in PM MnO to the experimental spectra [75]. The CT effect in  $2p$  XPS is known to be weaker in MnO compared to NiO and CoO [73,75–77]. This fact is reproduced by the present result as well as previous CM calculations [73,76]. To simulate the NLS effect, we have performed a calculation with hybridization density where the low-energy peak was artificially removed; see Figs. 5(b) and 5(c). In the simulated spectrum, the CT satellite is almost identical to the full calculation, while the low  $E_B$  side of the ML is enhanced leading to a discrepancy with the experiment. To our knowledge, the ML features in  $Mn^{2+}$  have not been discussed in the context of NLS so far. Very recently, Higashiya *et al.* [78] performed hard-x-ray photoelectron spectroscopy (HAXPES) measurements for  $LaOMnAs$  and  $(LaO)_{0.7}MnAs$  and found a sharp change in the Mn  $2p_{3/2}$  ML structure upon hole doping, which calls for a theoretical explanation.

### D. $V_2O_3$

Unlike the Mott insulators studied so far,  $V_2O_3$  is a paramagnetic metal under ambient conditions. In Fig. 6(a) we compare the V  $2p$  XPS with the experimental spectra of Ref. [79]. The  $2p_{3/2}$  ML shows a characteristic broadband structure with several shoulders. To analyze the origin of the shoulders, Figs. 6(c) and 6(d) show hybridization densities

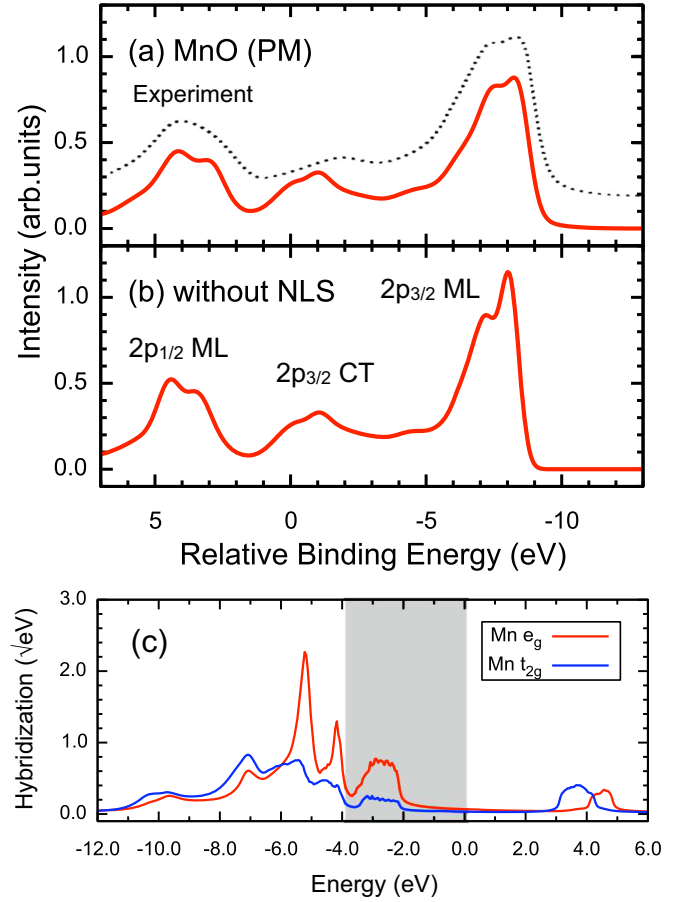


FIG. 5. (a) Mn  $2p$  XPS in MnO calculated by the DMFT framework. The experimental data (dashed) are taken from Ref. [75]. (b) Simulated spectrum ignoring the NLS. The spectral broadening is considered, using a Gaussian of 0.4 eV width (HWHM). (c) The hybridization densities between the impurity Mn  $3d$  and the (host) valence states.

$V(\epsilon)$  and valence spectral densities, respectively. In Fig. 6(d), the lower Hubbard band, the upper Hubbard band, and the coherent peak at the chemical potential are obtained. The coherent peak is characteristic for correlated metals [26,80]. In addition to hybridization with the main O  $2p$  band,  $V(\epsilon)$  in Fig. 6(c) exhibits three small peaks corresponding to the hybridization of V  $3d$  states on the impurity site with the Hubbard bands and the coherent peak. Although these features appear negligible compared to the O  $2p$  peak, the charge screening from their part below  $E_F$  is responsible for the width and shape of the V  $2p_{3/2}$  ML. Indeed, the shoulders disappear if the hybridization density above  $-4.0$  eV is artificially removed in the spectral calculation, as shown in Fig. 6(b) [81]. Therefore, the V  $2p$  XPS is quite sensitive to the fine features near  $E_F$ .

### E. $Fe_2O_3$

Figure 7(a) shows the Fe  $2p$  XPS in  $Fe_2O_3$  in the AF and PM phase. The overall structure of the spectra agrees well with experiments [11,82,83]. The interpretation of the Fe  $2p_{3/2}$  XPS in  $Fe_2O_3$  so far has been controversial. Droubay *et al.* [82] observed a double-peak feature in the Fe  $2p_{3/2}$  ML, whereas

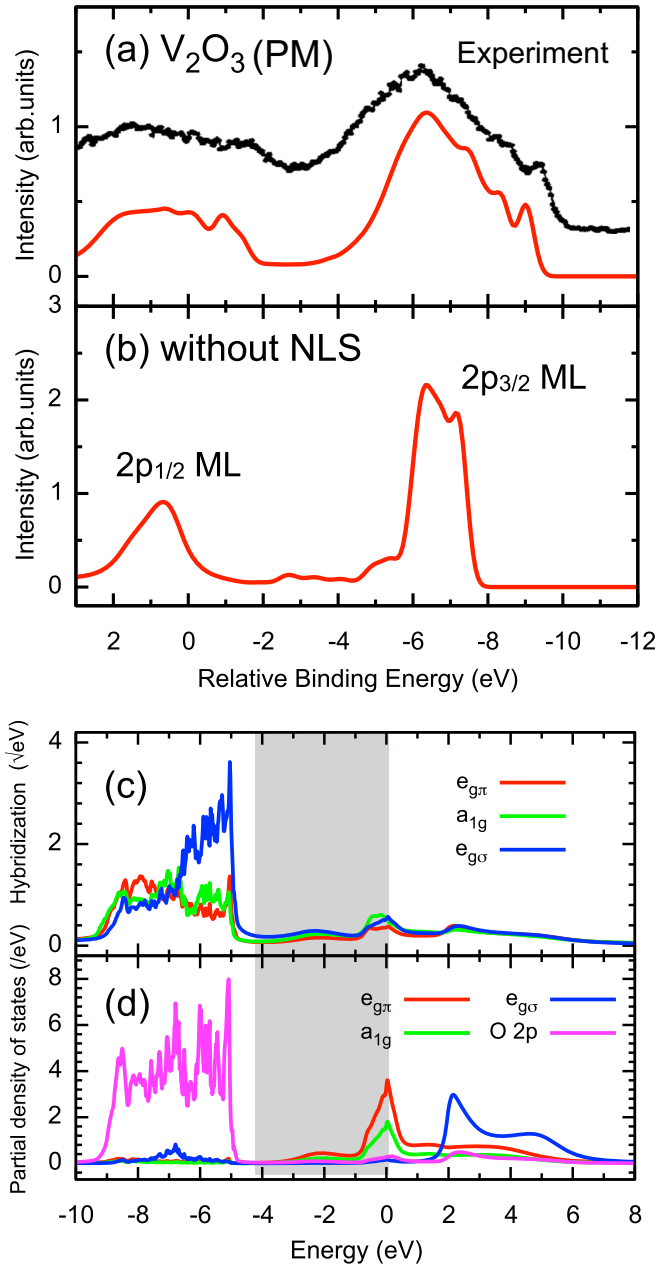


FIG. 6. (a) V 2p XPS spectra in V<sub>2</sub>O<sub>3</sub> calculated by the DMFT framework. The experimental data are taken from Ref. [79]. (b) Simulated spectrum ignoring the NLS. The spectral broadening is considered using a Gaussian of 0.25 eV width (HWHM). (c) Hybridization densities and (d) valence spectral intensities.

Fujii *et al.* [83] observed a broad structure in the ML. This ambiguity of ML might be caused by surface effects inherent to soft-x-ray experiments. However, the double-peak feature was observed also in recent bulk-sensitive HAXPES experiments by Miedema *et al.* [11], but it could not be explained by their CM analysis and therefore was attributed to extrinsic effects.

Our result in Fig. 7(a) reproduces the double-peak structure of the 2p<sub>3/2</sub> ML, in good agreement with the HAXPES data [11], suggesting that it is an intrinsic effect. We attribute the low  $E_B$  part of the ML to the NLS from the Fe 3d bands. In Fig. 7(b) we show the spectra without the NLS from Fe 3d bands obtained by artificially removing the shaded area of

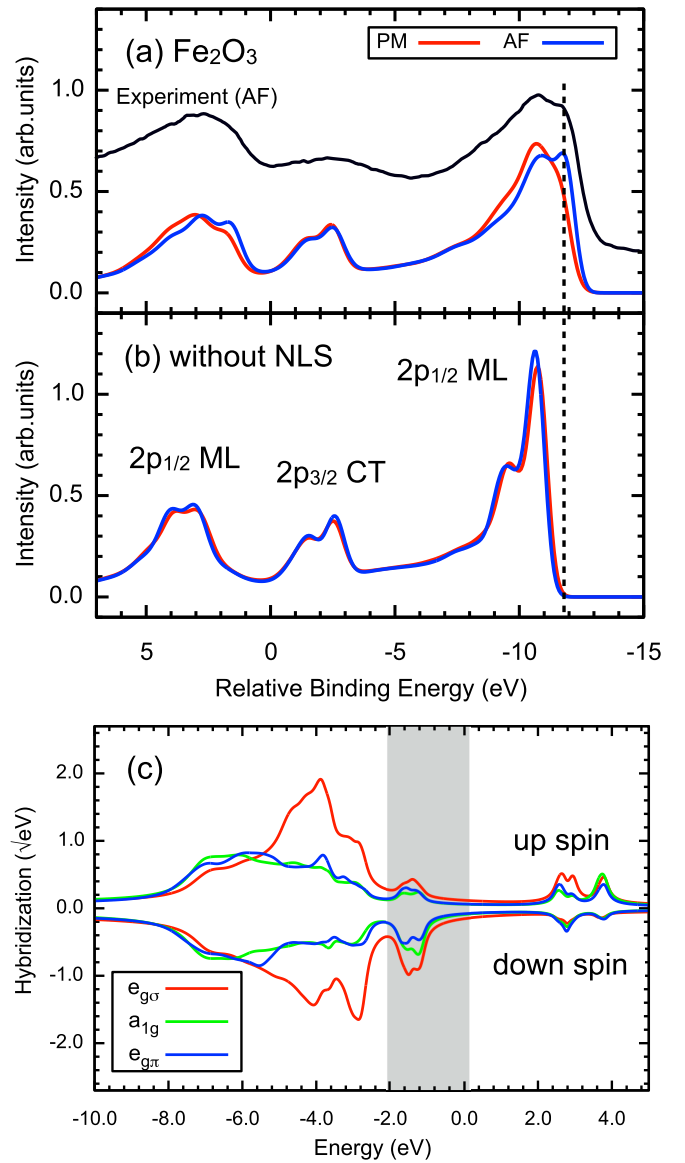


FIG. 7. (a) Fe 2p XPS spectra in Fe<sub>2</sub>O<sub>3</sub> for the AF and PM phase calculated by the DMFT framework. The experimental data are taken from Ref. [11]. (b) Simulated spectra ignoring the NLS effect from the Fe 3d band. The spectral broadening is considered using a Gaussian of 0.4 eV width (HWHM). (c) The hybridization densities between the impurity Fe 3d and the (host) valence states for the up-spin unit in the AF phase.

Fig. 7(c) from the hybridization density. Thus the simulated Fe 2p<sub>3/2</sub> ML consists of a sharp peak with a high- $E_B$  shoulder (multiplet effect), while the low- $E_B$  peak disappears [84]. Our result shows that the double-peak feature observed in the HAXPES experiments is an intrinsic feature of Fe<sub>2</sub>O<sub>3</sub>. In the PM phase, the low  $E_B$  peak is suppressed relative to the AF spectrum. This suggests that the mechanism of polarization-dependent NLS similar to NiO is in effect also in Fe<sub>2</sub>O<sub>3</sub>.

#### F. Cr<sub>2</sub>O<sub>3</sub> and LaCrO<sub>3</sub>

Finally, we discuss two Cr compounds with Cr<sup>3+</sup> valency Cr<sub>2</sub>O<sub>3</sub> and LaCrO<sub>3</sub>. The compounds are AF and PM at

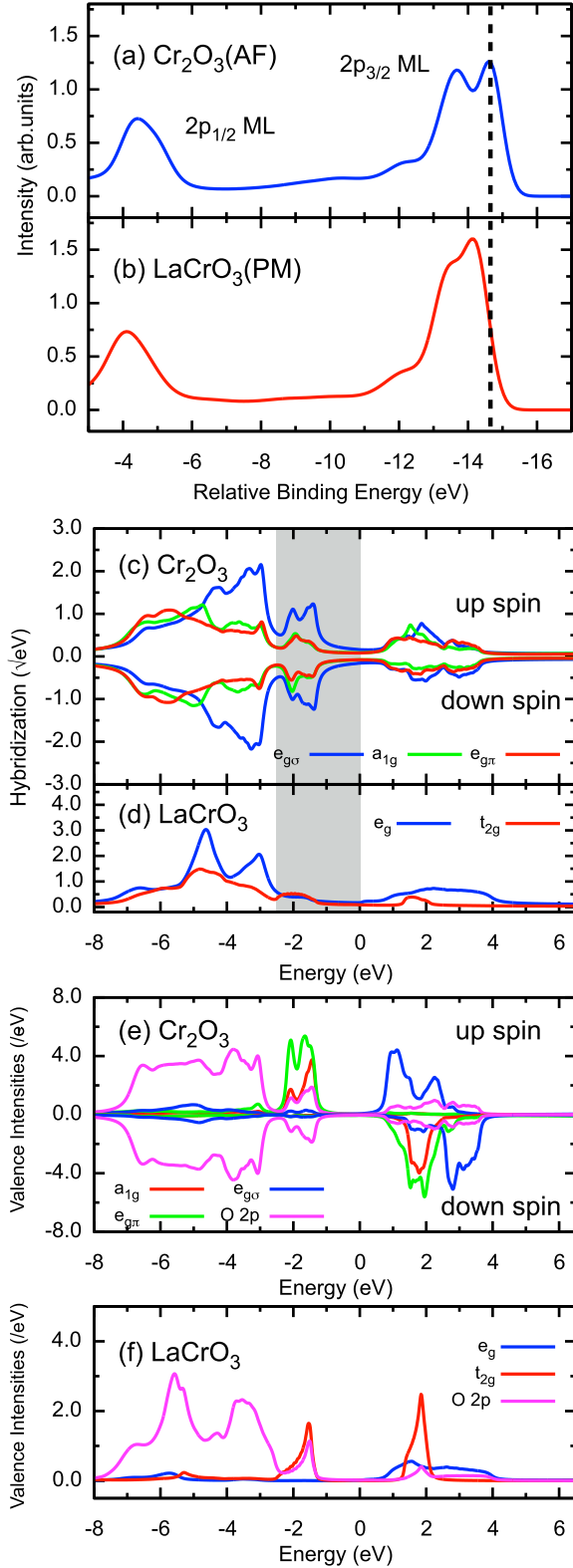


FIG. 8. Cr 2p XPS spectrum in (a) Cr<sub>2</sub>O<sub>3</sub> in AF phase and (b) LaCrO<sub>3</sub> in PM phase calculated by the DMFT framework. The spectral broadening is considered using a Gaussian of 0.4 eV width (HWHM). The hybridization densities between the impurity Cr 3d state and the (host) valence states in (c) Cr<sub>2</sub>O<sub>3</sub> and (d) LaCrO<sub>3</sub>. Valence spectral intensities calculated for (e) Cr<sub>2</sub>O<sub>3</sub> and (f) LaCrO<sub>3</sub>.

room temperature, respectively. In Fig. 8(a) we compare their calculated Cr 2p XPS. The overall shape of the spectra is consistent with the soft-x-ray experiments [85]. Despite their almost identical calculated Cr 3d charge states and gaps, the Cr 2p<sub>3/2</sub> MLs have different shapes.

To explain the different 2p<sub>3/2</sub> MLs, one needs to understand the relationship of the NLS to the crystal geometry. In both compounds, the Cr  $t_{2g}$  orbitals are half-filled. In LaCrO<sub>3</sub>, the NLS originates in the occupied  $t_{2g}$  states on the neighboring Cr atoms, while the empty  $e_g$  states cannot contribute [86]. The NLS from the  $t_{2g}$  states occurs via the  $\pi\pi$  path, which is quite weak in the perovskite structure. On the other hand, in Cr<sub>2</sub>O<sub>3</sub> with the corundum structure, the  $t_{2g}$  states on neighboring Cr sites contribute the NLS to the  $e_{g\sigma}$  states on the excited Cr site via a  $\pi\sigma$  path, which is stronger than the  $\pi\pi$  path in LaCrO<sub>3</sub>. This point is quantified in Figs. 8(c) and 8(d). The hybridization densities at low  $E_B$  exhibit a pronounced difference with the LaCrO<sub>3</sub> one being substantially smaller than the Cr<sub>2</sub>O<sub>3</sub> one. As a result, the LaCrO<sub>3</sub> spectrum is relatively well described by the CM, while in the Cr<sub>2</sub>O<sub>3</sub> spectrum NLS plays an important role. This demonstrates the sensitivity of the core-level XPS to the crystal geometry facilitated mainly by the NLS. HAXPES measurements on Cr<sub>2</sub>O<sub>3</sub> and LaCrO<sub>3</sub> as well as their doped versions are highly desirable to test our findings.

#### IV. CONCLUSIONS AND OUTLOOK

We have presented a systematic LDA+DMFT-based computational study of 2p core-level XPS in typical 3d transition metal oxides. Our study was able to accurately reproduce the fine features observed in high-resolution experiments. The nonlocal screening from 3d states on the TM neighbors of the excited atom, absent in conventional analysis using the cluster model, was shown to be crucial for a quantitative description of the studied spectra. Our results show that the core-level XPS is sensitive to generically nonlocal effects such as lattice geometry or magnetic order. However, to disentangle the nonlocal effects from the atomic multiplet effects in XPS, theoretical simulations such as the present one are necessary. A combined theoretical and experimental investigation of core-level XPS may provide insights into the physics of other classes of materials such as correlated metals, 4d and 5d materials with strong valence SO interaction, or materials with more complicated geometries.

#### ACKNOWLEDGMENTS

The authors thank F. de Groot, M. Ghiasi, J. Kolorenč, M. Taguchi, M. Mizumaki, A. Sekiyama, H. Fujiwara, T. Saitoh, M. Okawa, V. Pokorný, A. Sotnikov, and J. Fernández Afonso for fruitful discussions. A.H. thanks Y. Kawano, T. Yamamoto, Y. Ichinozuka, A. Yamanaka, and K. Nakanishi for valuable discussions. A.H. and J.K. are supported by the European Research Council (ERC) under the European Union's Horizon 2020 research and innovation programme (Grant Agreement No. 646807-EXMAG), and T.U. is supported by JSPS KAKENHI Grant No. JP16K05407.

- [1] M. Imada, A. Fujimori, and Y. Tokura, *Rev. Mod. Phys.* **70**, 1039 (1998).
- [2] D. I. Khomskii, *Transition Metal Compounds* (Cambridge University Press, Cambridge, 2014).
- [3] F. de Groot and A. Kotani, *Core Level Spectroscopy of Solids* (CRC, Boca Raton, FL, 2014).
- [4] M. Taguchi and G. Panaccione, Depth-Dependence of Electron Screening, Charge Carriers and Correlation: Theory and Experiments, in *Hard X-ray Photoelectron Spectroscopy (HAXPES)*, edited by J. C. Woicik (Springer International Publishing, Cham, Switzerland, 2016), pp. 197–216.
- [5] M. Taguchi, M. Matsunami, Y. Ishida, R. Eguchi, A. Chainani, Y. Takata, M. Yabashi, K. Tamasaku, Y. Nishino, T. Ishikawa, Y. Senba, H. Ohashi, and S. Shin, *Phys. Rev. Lett.* **100**, 206401 (2008).
- [6] R. Eguchi, M. Taguchi, M. Matsunami, K. Horiba, K. Yamamoto, Y. Ishida, A. Chainani, Y. Takata, M. Yabashi, D. Miwa, Y. Nishino, K. Tamasaku, T. Ishikawa, Y. Senba, H. Ohashi, Y. Muraoka, Z. Hiroi, and S. Shin, *Phys. Rev. B* **78**, 075115 (2008).
- [7] M. Obara, A. Sekiyama, S. Imada, J. Yamaguchi, T. Miyamachi, T. Balashov, W. Wulfhekkel, M. Yabashi, K. Tamasaku, A. Higashiya, T. Ishikawa, K. Fujiwara, H. Takagi, and S. Suga, *Phys. Rev. B* **81**, 113107 (2010).
- [8] M. Taguchi, A. Chainani, M. Matsunami, R. Eguchi, Y. Takata, M. Yabashi, K. Tamasaku, Y. Nishino, T. Ishikawa, S. Tsuda, S. Watanabe, C.-T. Chen, Y. Senba, H. Ohashi, K. Fujiwara, Y. Nakamura, H. Takagi, and S. Shin, *Phys. Rev. Lett.* **104**, 106401 (2010).
- [9] K. Horiba, M. Taguchi, A. Chainani, Y. Takata, E. Ikenaga, D. Miwa, Y. Nishino, K. Tamasaku, M. Awaji, A. Takeuchi, M. Yabashi, H. Namatame, M. Taniguchi, H. Kumigashira, M. Oshima, M. Lippmaa, M. Kawasaki, H. Koinuma, K. Kobayashi, T. Ishikawa, and S. Shin, *Phys. Rev. Lett.* **93**, 236401 (2004).
- [10] N. Kamakura, M. Taguchi, A. Chainani, Y. Takata, K. Horiba, K. Yamamoto, K. Tamasaku, Y. Nishino, D. Miwa, E. Ikenaga, M. Awaji, A. Takeuchi, H. Ohashi, Y. Senba, H. Namatame, M. Taniguchi, T. Ishikawa, K. Kobayashi, and S. Shin, *Europhys Lett.* **68**, 557 (2004).
- [11] P. Miedema, F. Borgatti, F. Offi, G. Panaccione, and F. de Groot, *J. Electron. Spectrosc. Relat. Phenom.* **203**, 8 (2015).
- [12] L. J. P. Ament, M. van Veenendaal, T. P. Devereaux, J. P. Hill, and J. van den Brink, *Rev. Mod. Phys.* **83**, 705 (2011).
- [13] G. Ghiringhelli, A. Piazzalunga, X. Wang, A. Bendounan, H. Berger, F. Bottegoni, N. Christensen, C. Dallera, M. Grioni, J.-C. Grivel, M. Moretti Sala, L. Patthey, J. Schlappa, T. Schmitt, V. Strocov, and L. Braicovich, *Eur. Phys. J. Spec. Top.* **169**, 199 (2009).
- [14] M. Guarise, B. D. Piazza, M. Moretti Sala, G. Ghiringhelli, L. Braicovich, H. Berger, J. N. Hancock, D. van der Marel, T. Schmitt, V. N. Strocov, L. J. P. Ament, J. van den Brink, P.-H. Lin, P. Xu, H. M. Rønnow, and M. Grioni, *Phys. Rev. Lett.* **105**, 157006 (2010).
- [15] J. Kim, D. Casa, M. H. Upton, T. Gog, Y.-J. Kim, J. F. Mitchell, M. van Veenendaal, M. Daghofer, J. van den Brink, G. Khaliullin, and B. J. Kim, *Phys. Rev. Lett.* **108**, 177003 (2012).
- [16] M. Minola, G. Dellea, H. Gretarsson, Y. Y. Peng, Y. Lu, J. Porras, T. Loew, F. Yakhov, N. B. Brookes, Y. B. Huang, J. Pellicciari, T. Schmitt, G. Ghiringhelli, B. Keimer, L. Braicovich, and M. L. Tacon, *Phys. Rev. Lett.* **114**, 217003 (2015).
- [17] J. Zaanen, C. Westra, and G. A. Sawatzky, *Phys. Rev. B* **33**, 8060 (1986).
- [18] K. Okada and A. Kotani, *J. Phys. Soc. Jpn.* **60**, 772 (1991).
- [19] A. E. Bocquet, T. Mizokawa, K. Morikawa, A. Fujimori, S. R. Barman, K. Maiti, D. D. Sarma, Y. Tokura, and M. Onoda, *Phys. Rev. B* **53**, 1161 (1996).
- [20] A. Agui, T. Uozumi, M. Mizumaki, and T. Käämbre, *Phys. Rev. B* **79**, 092402 (2009).
- [21] M. A. van Veenendaal and G. A. Sawatzky, *Phys. Rev. Lett.* **70**, 2459 (1993).
- [22] M. van Veenendaal, *Phys. Rev. B* **74**, 085118 (2006).
- [23] A. Hariki, Y. Ichinozuka, and T. Uozumi, *J. Phys. Soc. Jpn.* **82**, 043710 (2013).
- [24] A. Hariki, A. Yamanaka, and T. Uozumi, *Europhys Lett.* **114**, 27003 (2016).
- [25] W. Metzner and D. Vollhardt, *Phys. Rev. Lett.* **62**, 324 (1989).
- [26] A. Georges, G. Kotliar, W. Krauth, and M. J. Rozenberg, *Rev. Mod. Phys.* **68**, 13 (1996).
- [27] A. Hariki, Y. Ichinozuka, and T. Uozumi, *J. Phys. Soc. Jpn.* **82**, 023709 (2013).
- [28] G. Kotliar, S. Y. Savrasov, K. Haule, V. S. Oudovenko, O. Parcollet, and C. A. Marianetti, *Rev. Mod. Phys.* **78**, 865 (2006).
- [29] J. Kuneš, I. Leonov, M. Kollar, K. Byczuk, V. I. Anisimov, and D. Vollhardt, *Eur. Phys. J. Spec. Top.* **180**, 5 (2009).
- [30] A. Hariki, A. Yamanaka, and T. Uozumi, *J. Phys. Soc. Jpn.* **84**, 073706 (2015).
- [31] A. Georges and G. Kotliar, *Phys. Rev. B* **45**, 6479 (1992).
- [32] P. Blaha, K. Schwarz, G. Madsen, D. Kvasnicka, and J. Luitz, *WIEN2k, An Augmented Plane Wave + Local Orbitals Program for Calculating Crystal Properties* (Karlheinz Schwarz, Techn. Universitat Wien, Austria, 2001).
- [33] J. Kuneš, R. Arita, P. Wissgott, A. Toschi, H. Ikeda, and K. Held, *Comput. Phys. Commun.* **181**, 1888 (2010).
- [34] A. A. Mostofi, J. R. Yates, G. Pizzi, Y.-S. Lee, I. Souza, D. Vanderbilt, and N. Marzari, *Comput. Phys. Commun.* **185**, 2309 (2014).
- [35] P. Werner, A. Comanac, L. de' Medici, M. Troyer, and A. J. Millis, *Phys. Rev. Lett.* **97**, 076405 (2006).
- [36] E. Gull, A. J. Millis, A. I. Lichtenstein, A. N. Rubtsov, M. Troyer, and P. Werner, *Rev. Mod. Phys.* **83**, 349 (2011).
- [37] L. Boehnke, H. Hafermann, M. Ferrero, F. Lechermann, and O. Parcollet, *Phys. Rev. B* **84**, 075145 (2011).
- [38] H. Hafermann, K. R. Patton, and P. Werner, *Phys. Rev. B* **85**, 205106 (2012).
- [39] E. Pavarini, E. Koch, D. Vollhardt, and A. Lichtenstein, *The LDA+DMFT Approach to Strongly Correlated Materials* (Verlag des Forschungszentrum, Jülich, 2014).
- [40] V. Křápek, P. Novák, J. Kuneš, D. Novoselov, D. M. Korotin, and V. I. Anisimov, *Phys. Rev. B* **86**, 195104 (2012).
- [41] M. Jarrell and J. Gubernatis, *Phys. Rep.* **269**, 133 (1996).
- [42] X. Wang, E. Gull, L. de' Medici, M. Capone, and A. J. Millis, *Phys. Rev. B* **80**, 045101 (2009).
- [43] M. Matsubara, T. Uozumi, A. Kotani, and J. C. Parlebas, *J. Phys. Soc. Jpn.* **74**, 2052 (2005).
- [44] V. I. Anisimov, J. Zaanen, and O. K. Andersen, *Phys. Rev. B* **44**, 943 (1991).
- [45] D. Korotin, A. V. Kozhevnikov, S. L. Skornyakov, I. Leonov, N. Binggeli, V. I. Anisimov, and G. Trimarchi, *Eur. Phys. J. B* **65**, 91 (2008).



- [46] L. Vaugier, H. Jiang, and S. Biermann, *Phys. Rev. B* **86**, 165105 (2012).
- [47] K. Held, G. Keller, V. Eyert, D. Vollhardt, and V. I. Anisimov, *Phys. Rev. Lett.* **86**, 5345 (2001).
- [48] H. T. Dang, X. Ai, A. J. Millis, and C. A. Marianetti, *Phys. Rev. B* **90**, 125114 (2014).
- [49] T. Uozumi, K. Okada, A. Kotani, R. Zimmermann, P. Steiner, S. Hüfner, Y. Tezuka, and S. Shin, *J. Electron. Spectrosc. Relat. Phenom.* **83**, 9 (1997).
- [50] J. C. Slater, *Quantum Theory of Atomic Structure* (McGraw-Hill, California, 1960), Vol. 1.
- [51] R. D. Cowan, *The Theory of Atomic Structure and Spectra (Los Alamos Series in Basic and Applied Sciences)* (University of California Press, New York, 1981).
- [52] J. Sugar, *Phys. Rev. B* **5**, 1785 (1972).
- [53] A. Tanaka and T. Jo, *J. Phys. Soc. Jpn.* **61**, 2040 (1992).
- [54] F. M. F. de Groot, J. C. Fuggle, B. T. Thole, and G. A. Sawatzky, *Phys. Rev. B* **42**, 5459 (1990).
- [55] A. E. Bocquet, T. Mizokawa, T. Saitoh, H. Namatame, and A. Fujimori, *Phys. Rev. B* **46**, 3771 (1992).
- [56] J. Park, S. Ryu, M.-s. Han, and S.-J. Oh, *Phys. Rev. B* **37**, 10867 (1988).
- [57] See Supplemental Material at <http://link.aps.org/supplemental/10.1103/PhysRevB.96.045111> for the complete set of computational parameters as well as the valance spectral and hybridization intensities of the studied compounds. The Supplemental Material includes Refs. [3,44,87–94].
- [58] Q. Yin, A. Gordienko, X. Wan, and S. Y. Savrasov, *Phys. Rev. Lett.* **100**, 066406 (2008).
- [59] R. Eder, *Phys. Rev. B* **76**, 241103 (2007).
- [60] J. Kuneš, V. I. Anisimov, S. L. Skornyakov, A. V. Lukoyanov, and D. Vollhardt, *Phys. Rev. Lett.* **99**, 156404 (2007).
- [61] J. Kuneš, V. I. Anisimov, A. V. Lukoyanov, and D. Vollhardt, *Phys. Rev. B* **75**, 165115 (2007).
- [62] R. Eder, *Phys. Rev. B* **78**, 115111 (2008).
- [63] L. Huang, Y. Wang, and X. Dai, *Phys. Rev. B* **85**, 245110 (2012).
- [64] A. A. Dyachenko, A. O. Shorikov, A. V. Lukoyanov, and V. I. Anisimov, *JETP Lett.* **96**, 56 (2012).
- [65] J. Kuneš, A. V. K. Lukoyanov, R. T. Scalettar, and W. E. Pickett, *Nat. Mater.* **7**, 198 (2008).
- [66] I. Leonov, L. Pourovskii, A. Georges, and I. A. Abrikosov, *Phys. Rev. B* **94**, 155135 (2016).
- [67] I. Leonov, V. I. Anisimov, and D. Vollhardt, *Phys. Rev. B* **91**, 195115 (2015).
- [68] A. I. Poteryaev, J. M. Tomczak, S. Biermann, A. Georges, A. I. Lichtenstein, A. N. Rubtsov, T. Saha-Dasgupta, and O. K. Andersen, *Phys. Rev. B* **76**, 085127 (2007).
- [69] P. Hansmann, A. Toschi, G. Sangiovanni, T. Saha-Dasgupta, S. Lupi, M. Marsi, and K. Held, *Physica Status Solidi B* **250**, 1251 (2013).
- [70] Note that the  $S$  and  $S_z$  are not exact conserved quantities due to the SO interaction, but they are still suitable to characterize the system.
- [71] A. Chainani, T. Yokoya, Y. Takata, K. Tamasaku, M. Taguchi, T. Shimojima, N. Kamakura, K. Horiba, S. Tsuda, S. Shin, D. Miwa, Y. Nishino, T. Ishikawa, M. Yabashi, K. Kobayashi, H. Namatame, M. Taniguchi, K. Takada, T. Sasaki, H. Sakurai, and E. Takayama-Muromachi, *Phys. Rev. B* **69**, 180508 (2004).
- [72] Z.-X. Shen, J. W. Allen, P. A. P. Lindberg, D. S. Dessau, B. O. Wells, A. Borg, W. Ellis, J. S. Kang, S.-J. Oh, I. Lindau, and W. E. Spicer, *Phys. Rev. B* **42**, 1817 (1990).
- [73] K. Okada and A. Kotani, *J. Phys. Soc. Jpn.* **61**, 4619 (1992).
- [74] F. de Groot, *Coordin. Chem. Rev.* **249**, 31 (2005).
- [75] P. S. Bagus, R. Broer, W. A. de Jong, W. C. Nieuwpoort, F. Parmigiani, and L. Sangaletti, *Phys. Rev. Lett.* **84**, 2259 (2000).
- [76] M. Taguchi, T. Uozumi, and A. Kotani, *J. Phys. Soc. Jpn.* **66**, 247 (1997).
- [77] P. S. Bagus and E. S. Ilton, *Phys. Rev. B* **73**, 155110 (2006).
- [78] A. Higashiya, K. Nakagawa, A. Yamasaki, K. Nagai, S. Fujioka, Y. Kanai, K. Yamagami, H. Fujiwara, A. Sekiyama, A. Abozeed, T. Kadono, S. Imada, K. Kuga, M. Yabashi, K. Tamasaku, T. Ishikawa, S. Toyama, and K. Takase, *J. Electron. Spectrosc. Relat. Phenom.* (to be published).
- [79] M. Taguchi, A. Chainani, N. Kamakura, K. Horiba, Y. Takata, M. Yabashi, K. Tamasaku, Y. Nishino, D. Miwa, T. Ishikawa, S. Shin, E. Ikenaga, T. Yokoya, K. Kobayashi, T. Mochiku, K. Hirata, and K. Motoya, *Phys. Rev. B* **71**, 155102 (2005).
- [80] G. Keller, K. Held, V. Eyert, D. Vollhardt, and V. I. Anisimov, *Phys. Rev. B* **70**, 205116 (2004).
- [81] The higher  $E_B$  side also loses spectral weight, which can be understood by a similar argument as in Sec. II A, i.e., the locally and nonlocally screened states repel each other due to virtual hopping via the unscreened state.
- [82] T. Droubay and S. A. Chambers, *Phys. Rev. B* **64**, 205414 (2001).
- [83] T. Fujii, F. M. F. de Groot, G. A. Sawatzky, F. C. Voogt, T. Hibma, and K. Okada, *Phys. Rev. B* **59**, 3195 (1999).
- [84] The  $2p_{3/2}$  ML of the simulated spectra is similar to the CM result of Ref. [11].
- [85] L. Qiao, H. Y. Xiao, S. M. Heald, M. E. Bowden, T. Varga, G. J. Exarhos, M. D. Biegalski, I. N. Ivanov, W. J. Weber, T. C. Droubay, and S. A. Chambers, *J. Mater. Chem. C* **1**, 4527 (2013).
- [86] Note that local screening from the neighboring oxygen  $2p$  states to the  $e_g$  states is possible.
- [87] J. Hugel and M. Kamal, *Solid State Commun.* **100**, 457 (1996).
- [88] W. Neubeck, C. Vettier, V. Fernandez, F. de Bergevin, and C. Giles, *J. Appl. Phys.* **85**, 4847 (1999).
- [89] A. K. Cheetham and D. A. O. Hope, *Phys. Rev. B* **27**, 6964 (1983).
- [90] B. E. F. Fender, A. J. Jacobson, and F. A. Wegwood, *J. Chem. Phys.* **48**, 990 (1968).
- [91] H. A. Alperin, *J. Phys. Soc. Jpn. Suppl. B* **17**, 12 (1962).
- [92] D. C. Khan and R. A. Erickson, *Phys. Rev. B* **1**, 2243 (1970).
- [93] D. Herrmann-Ronzaud, P. Burlet, and J. Rossat-Mignod, *J. Phys. C* **11**, 1213 (1978).
- [94] O. Gunnarsson and K. Schönhammer, *Phys. Rev. B* **28**, 4315 (1983).